

Single-frame label-free cell tomography at speed of more than 10,000 volumes per second

Baoliang Ge^{1,2,†}, Yanping He^{3,†}, Mo Deng^{1,†}, Md Habibur Rahman³, Yijin Wang³, Ziling Wu¹, Chung Hong N. Wong^{4,5}, Michael K. Chan^{4,5}, Yi-Ping Ho^{3,5,6}, Liting Duan³, Zahid Yaqoob², Peter T. C. So^{1,2,7,8,*}, George Barbastathis^{1,8,9,*}, and Renjie Zhou^{3,*}

¹Department of Mechanical Engineering, Massachusetts Institute of Technology, Cambridge, MA 02139, USA

²Laser Biomedical Research Center, Massachusetts Institute of Technology, Cambridge, MA 02139, USA

³Department of Biomedical Engineering, The Chinese University of Hong Kong, Shatin, New Territories, Hong Kong SAR, China

⁴School of Life Sciences, The Chinese University of Hong Kong, Shatin, New Territories, Hong Kong SAR, China

⁵Centre for Novel Biomaterials, The Chinese University of Hong Kong, Shatin, New Territories, Hong Kong SAR, China

⁶Hong Kong Branch of CAS Center for Excellence in Animal Evolution and Genetics, The Chinese University of Hong Kong, Shatin, New Territories, Hong Kong SAR, China

⁷Department of Biological Engineering, Massachusetts Institute of Technology, Cambridge, MA 02139, USA

⁸Interdisciplinary Research Group on Critical Analytics for Manufacturing Personalized medicine (CAMP), Singapore-MIT Alliance for Research and Technology Centre, Singapore

⁹Intra-Create Thematic Grant on Retinal Analytics through Machine learning aiding Physics (RAMP), Singapore-MIT Alliance for Research and Technology Centre, Singapore

[†]These authors contributed equally to this work

*Corresponding authors: ptso@mit.edu; gbarb@mit.edu; rjzhou@cuhk.edu.hk

Abstract: Three-dimensional (3D) image cytometers may significantly improve the cell analysis accuracy to facilitate biological discoveries and clinical diagnosis, but their development is curbed by the low imaging throughput. Here we report SIngle-frame LAbel-free Cell Tomography (SILACT) with diffraction-limited resolution and unprecedented imaging speed of over 10,000 volumes/second. SILACT is built on a unique interferometric microscope with angle-multiplexing illumination and a pre-trained physics-incorporating Deep Neural Network for efficient 3D Refractive Index (RI) reconstruction, from which 3D morphological and biophysical parameters of cells are extracted. With microfluidics and a high-speed camera, SILACT is capable of imaging over 20,000 cells/second and distinguishing different cell species during rapid measurements of large cell quantities, as well as visualizing shear-induced 3D transient deformation of red blood cells on a sub-millisecond scale.

One-Sentence Summary: Single-frame Label-free Cell Tomography (SILACT) is developed to image cells and their dynamics with diffraction-limited resolution and unprecedented imaging speed in excess of 10,000 volumes/second.

1. Introduction

High-throughput and high-content cell phenotyping has been widely applied in drug screening (1–3), clinical testing (4), and regenerative medicine (5) by enabling rapid characterization of large cell populations for morphological, mechanical, and other biophysical properties (6). Some of these properties have been recognized as important biomarkers for discerning the physiological and pathological states of cells (7–9). For example, by scrutinizing population composition changes of leukocytes based on their morphology, one may find indicators for immune systems failure or detect the presence of infectious diseases (10). Similarly, mechanical parameters extracted from measuring membrane fluctuations or deformations of Red Blood Cells (RBCs) (7, 11–13) have been deployed as biophysical biomarkers to investigate the etiology of malaria (14) and sickle cell disease (8). Further advances in high-speed live-cell analysis assays that can assess cellular properties more effectively, accurately, and noninvasively can broadly impact many areas of biomedical investigations and clinical applications.

Image cytometry (15–18) has recently emerged as a powerful tool for high-content cell-based assays with extremely high throughputs achieved in two-dimensional (2D) imaging approaches (18, 19). As cells have complex three-dimensional (3D) structures, 2D imaging methods are incapable of revealing intracellular structures and quantifying cellular morphologies as comprehensively and accurately as their 3D counterparts (15, 16, 20) (e.g., confocal microscopy (21), light-sheet microscopy (22, 23), structured illumination microscopy (24), and optical diffraction tomography (ODT) (25, 26)). However, 3D imaging methods usually require long scanning time and extensive data processing, their throughput is typically limited to <1,000 cells/second (16, 27) even when combined with faster scanning hardware (28, 29) and more effective reconstruction algorithms (30, 31). In addition, as mainstream 3D imaging methods are often fluorescence-based, photobleaching of fluorescent labels reduces image quality and prevents extended duration of visualization (32). Moreover, the use of fluorescent labels not only requires additional preparation steps but also may confound the interpretation by affecting cellular activities and structures (33, 34).

To meet the demand for high-throughput 3D image cytometry, we report an innovative approach called SIngle-frame LAbel-free Cell Tomography (SILACT). Instead of acquiring a large number of images (>50) at different illumination angles or sample depth-scanning positions (35)(36), in SILACT only a single interferogram that multiplexes four illumination angles is captured. Machine learning-driven computational imaging approaches have recently been applied to super-resolution imaging (37), image phase retrieval (38), low-photon imaging (39), virtual staining of biopsy specimens (40), etc. Here in SILACT, a fast 3D reconstruction algorithm based on a pre-trained physics-incorporating Deep Neural Network (DNN) is adopted to reliably reconstruct the 3D structures of cells with high spatial resolution by mapping their 3D refractive-index (RI) distributions from the acquired single interferogram.

With these innovations, in this work we demonstrate that SILACT can easily achieve a speed in excess of 10,000 volumes/second (vps) with a high-speed camera. Combined with customized microfluidic devices, SILACT can be operated as a 3D imaging cytometer with an

imaging throughput surpassing 20,000 cells/second. By segmenting the cells and extracting unique 3D morphological and biophysical parameters (i.e., volume, surface area, dry mass, and mean RI), we have shown that SILACT is able to distinguish different cell species during rapid measurements of large cell quantities. Furthermore, SILACT is applied to characterizing transient 3D deformations of RBCs induced by the shearing force in a microfluidic channel on the sub-millisecond scale, which showcases its potential for quantifying cell mechanical properties and monitoring ultra-fast cellular dynamics. With unique capabilities for high-speed label-free 3D cell analysis, we envision that SILACT may promote various cutting-edge biomedical studies and open new possibilities for novel diagnostic techniques.

2. Theory & Results

2.1 Overview of SILACT

The overall pipeline of SILACT, as illustrated in Fig. 1a, contains two key components: (i) an interferometric microscope with angle-multiplexing optics that simultaneously illuminates the samples from four angles; (ii) a Machine-Learning (ML) engine that converts a single interferogram containing four illumination angles of the cells to a 3D RI map, while compensating for missing spatial frequency information due to the use of only a few illumination angles. Since SILACT acquires volumetric information from a single 2D interferogram, the volumetric imaging rate is only limited by the camera frame rate and the number of photons received. With a high-speed camera and adequate illumination power that is safe to the cells, one can easily push the 3D acquisition speed to over 10,000 vps.

In SILACT, we implement an off-axis digital holography design for the interferometric microscope (25, 41). Multiplexing four illumination angles for single-frame 3D imaging is achieved by overlapping multiple Lee hologram patterns (42) on a Digital Micro-mirror Device (DMD). The details of the imaging system design are elaborated in *Methods*, Section 4.1. In the following sections, we will show that the utilisation of four angles strikes a good balance between acquisition time and reconstruction fidelity.

The ML engine reconstructs the 3D RI map of the sample as follows. First, the raw multiplex interferogram is pre-processed through a spectral filtering method to extract four Phase Approximants (see *Methods*, Section 4.2 and *Supplementary Material*, Section S1), which are essentially approximations of the quantitative phase delay accrued after the light has gone through the sample at each corresponding angle. The Phase Approximants are then input to a pre-trained DNN model (Fig. 1b (iii)) to infer the 3D RI maps. Thereafter, a linear fitting procedure is applied to recover the quantitative RI values (see *Methods*, Section 4.3).

Central to getting our SILACT method to work is the supervised training scheme for the ML engine. We first construct a dataset for training and testing our DNN model (Fig. 1b (i) and (ii)). For each cell, two types of raw data are acquired with our interferometric microscope-based imaging platform: (i) 49 sequential interferograms, each from a single scanning illumination angle; and (ii) a single-frame interferogram from illuminating the sample simultaneously with four beams with the same elevation angle and azimuthal angles at 0° , 90° , 180° , and 270° (refer to *Supplementary Material*, Section S1 for details on the angle scanning

patterns in each data type). Acquisition (i) is used to obtain the ground truth 3D RI maps of the cells for training, whereas acquisition (ii) is the normal operating mode of SILACT as described earlier.

The ground truth 3D RI maps are produced from acquisition (i) as follows: firstly, phase maps corresponding to each illumination angle are retrieved based on the Fourier transform method. The 49 phase maps are then used to reconstruct 3D RI maps using the Learning Tomography Beam Propagation Method (LT-BPM) (43, 44) (see *Supplementary Material*, Section 2). The reliability of LT-BPM as ground truth is validated on calibration samples, including polystyrene beads and 3D printed cell phantoms (see *Supplementary Material*, Sections S3). The DNN model is based on the Learning to Synthesize by DNN (LS-DNN) (45) principle, which here we generalize for 3D RI reconstruction (see *Methods*, Section 4.3). The supervised training procedure minimizes the Negative Pearson Correlation Coefficient (NPCC) loss (46) between the ground truth RI map and the output of the LS-DNN when its input are the Phase Approximants. The choice of NPCC is meant to further ensure the preservation of the sample's fine features. The key contribution of the LS-DNN scheme to our problem is to combat the uneven fidelity of low and high spatial frequencies that often occurs in DNN training (38). Thus, the spatial resolution of the final 3D RI maps can be greatly improved.

The DNN is trained with 900 pairs of ground truth RI maps and corresponding Phase Approximants extracted from raw multiplex interferograms of NIH/3T3 cells. The NIH/3T3 cells used for training are cultured on glass-bottom well plates. As the angle scanning speed is fast (i.e., at 5000 sec^{-1} during the data acquisition) and 49 angles are exploited for reconstruction, the cells can be considered static during one complete angle-scanning process. The ML-engine's ability to generalize beyond its training to different cell types is discussed further in Section 2.3. Moreover, after training, SILACT's ML engine is fast in inferring the 3D RI map from Phase Approximants, taking only 0.68 second/volume on average (refer to *Supplementary*, Section S5 for detailed analysis of computational time and comparison with exiting 3D RI reconstruction methods).

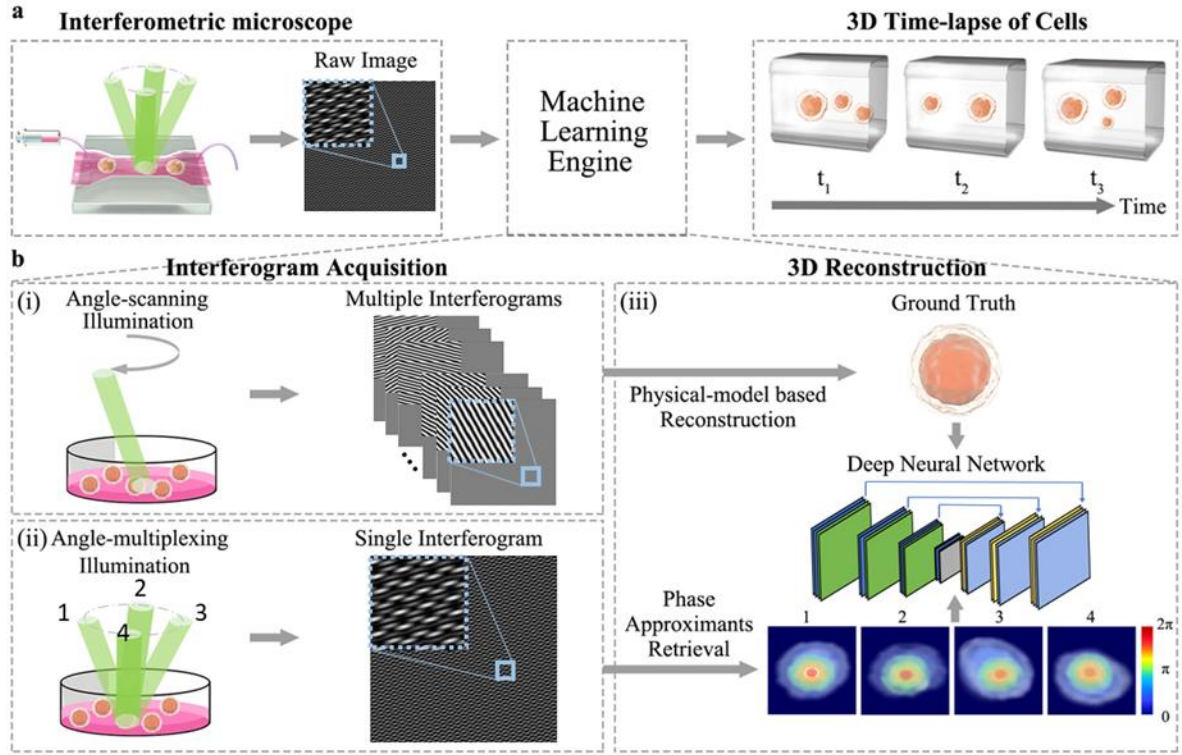


Figure 1. The overall working principle of SILACT. (a) The pipeline of 3D time-lapse imaging via SILACT consists of two principal steps: multiplex interferograms captured from the interferometric microscope and 3D RI map inference from a machine learning engine containing a Phase Approximant retrieval algorithm and a pre-trained DNN. (b) The training process of the machine learning engine for 3D reconstruction: (i) illustrates the acquisition of all 49 interferograms captured under the angle-scanning illumination scheme used for generating ground truth RI maps; (ii) shows the acquisition of the multiplex interferogram; and (iii) describes how the ground truth 3D RI maps (prepared using a physical-model based reconstruction algorithm, i.e., LT-BPM) and the four Phase Approximants (estimated from the multiplex interferogram) are used for training the DNN.

2.2 Quantitative validation of SILACT

We now turn to the validation of our design choices, namely: (i) the extent we can compress the number of angle-scanning measurements with deep learning; and (ii) the feasibility of multiplexing four illumination angles in one interferogram acquisition. The performance of LT-BPM (i.e., the physical model for acquiring the ground truth RI maps) with sequentially scanning illumination angles drops dramatically when image acquisition number decreases from 32 to 1 as shown in Fig. 2a-c, where Pearson Correlation Coefficient (PCC), Mean Absolute Error (MAE), and Root Mean Square Error (RMSE) are used for quantitative assessments by comparing with 49-angle LT-BPM. The loss of fidelity can be mitigated by applying deep learning. By pre-training a DNN using ground truth RI maps from LT-BPM with 49 scanning angles, we can predict the 3D RI maps of cells with compressed measurements. We call this method Multi-frame Deep-learning ODT (MDODT) (see *Supplementary Material*, Section S4). Even with only four scanning angles or four acquisitions, MDODT reconstruction results are almost indistinguishable from that of 32 image acquisitions with LT-BPM. However, reducing the number of illumination angles to one significantly deteriorates the performance.

Moving forward, we multiplex four illumination angles into one interferogram using a DMD in an angle-scanning interferometric microscope. With only one acquisition, it is found that the imaging performance is similar to MDODT when the number of imaging acquisitions is four, as shown in Fig. 2a-c. Therefore, our choice of multiplexing four illumination angles in SILACT is well justified. Note that multiplexing more than four illumination angles in SILACT may achieve similar performance, but this will require a new set of training data and re-train the DNN.

2.3 SILACT generalizability: 3D RI maps of diverse cell species

3D RI maps of various cell species are reconstructed with SILACT and shown in Fig. 2d-e. The y-z sections at the origin of the x-axis and x-y cross-sections at the centre layer and layers located $\pm 1 \mu\text{m}$ above and below are shown in different columns in Fig. 2d. 3D renderings of RI maps are also provided in Supplementary Videos 1-4. In Fig. 2e, the nucleoli, the nuclei's boundaries, and other organelles are readily distinguishable in the 3D renderings. Comparisons between SILACT and corresponding ground truth reconstructions of various cell species demonstrate the accuracy of SILACT (refer to *Supplementary Material*, section S6).

By applying this algorithm to other cell types and evaluating SILACT's reconstruction performance on different cell species, we can assess the generalizability of our approach. From the testing results measured with PCC, MAE, or RMSE, it is found that the generalization performance on several other similar eukaryotic cell species (HEK293T, HeLa, COS-7 cells) is comparable to the testing results of NIH/3T3 cells. The same applies when SILACT is tested on RBCs, a very different cell type without nuclei and organelles, as shown in *Supplementary Material*, section S9. The ability to generalize to other types of cells is remarkable, especially given that our ML engine is trained on only ~900 NIH/3T3 cells.

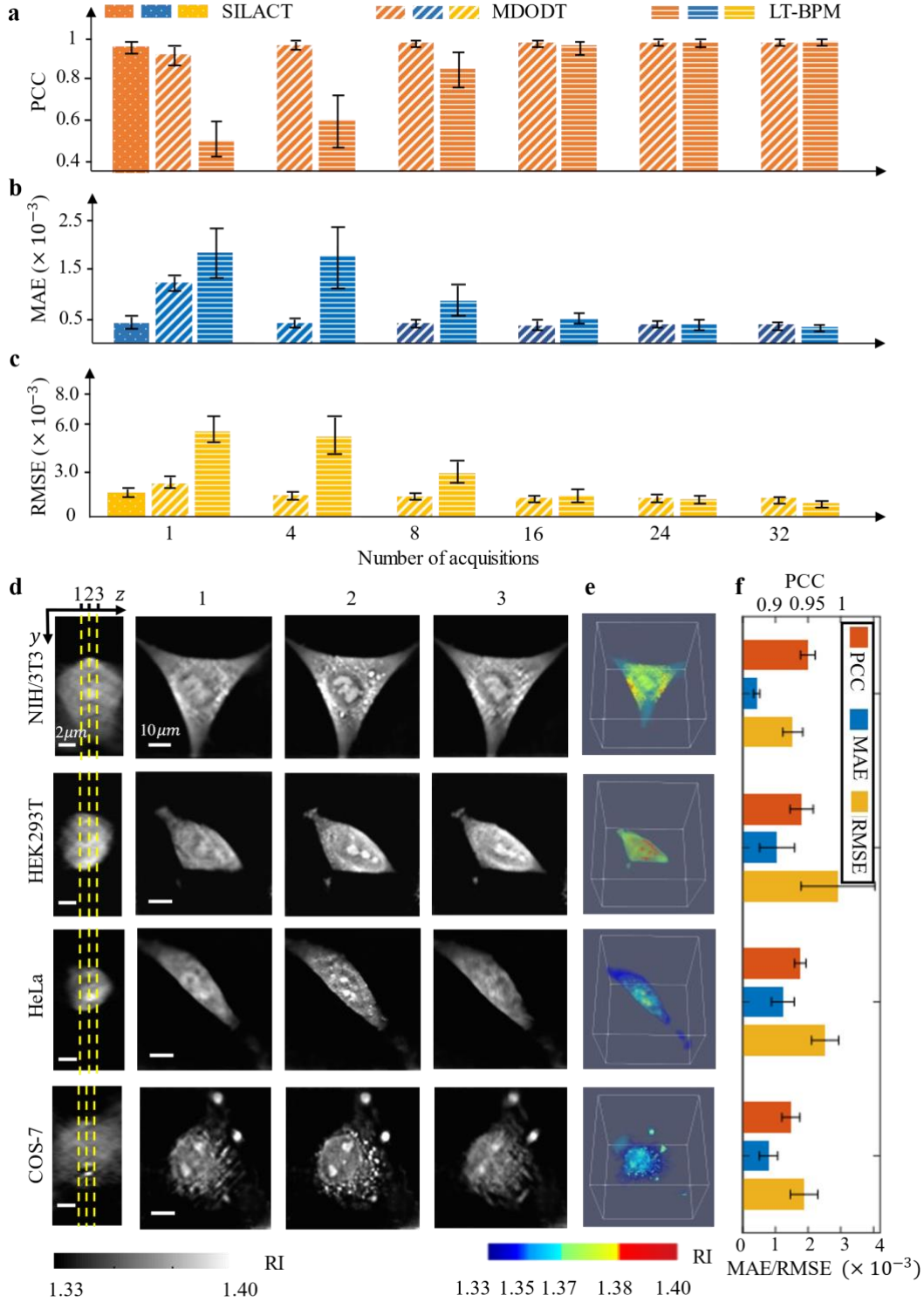


Figure 2. Evaluation of SILACT's performance. Comparison of quantitative metrics (a) PCC, (b) MAE, and (c) RMSE for SILACT, MDODT, and LT-BPM as a function of the number of acquisitions. (d)-(f), visualization and quantitative evaluation of predicted RI maps of NIH/3T3 cells, HEK293T cells, HeLa cells, and COS-7 cells by the SILACT algorithm. The first column of (d) shows the cross-sections of the 3D RI map on $y-z$ plane; The $x-y$ cross-sections at different z locations (1) $z_0 - 1\mu m$, (2) z_0 and (3) $z_0 + 1\mu m$ (identified with yellow dashed lines in the first column, where z_0 indicates the central plane) are shown in the second to fourth columns of (d), respectively. 3D renderings of the RI maps are shown in (e). The same quantitative metrics as in (a)-(c) are shown in (f). 3D rendering videos are provided in Supplementary Videos 1-4.

2.4 High-throughput and high-content 3D imaging flow cytometry

To operate SILACT in 3D imaging flow cytometer mode, we incorporate a high-speed camera and microfluidic devices (see *Supplementary Material*, Section S10). The speed of imaging that yields full 3D RI maps is 12,500 vps with 10-15 μ s exposure time. We demonstrate the utility of this system by injecting cells into microfluidic channels (refer to Fig. S9 c-e for the cross-sections of the channels). Three types of cell specimens are used with the following suspension and flow velocity conditions: NIH/3T3 cells with suspension at 20×10^6 cells/mL and flow velocity at 0.46 m/sec, Jurkat T cells with suspension at 90×10^6 cells/mL and flow velocity at 0.31 m/sec, and mouse RBCs with suspension at 100×10^6 cells/mL and flow velocity at 0.56 m/sec. 3D renderings of RI maps at different time points for flowing NIH/3T3 cells, Jurkat T cells, and mouse RBCs are shown in Fig. 3a-c, respectively. A total of 936 NIH/3T3 cells are acquired within 160 ms (equivalent to a throughput of approximately 5,580 cells/second) and rendered into a time-lapse video (Supplementary Video 5). The Jurkat T cells and mouse RBCs are prepared at a higher cell density to push the throughput limit. A total of 3,350 Jurkat T cells are captured within 160 ms (refer to the rendered time-lapse video in Supplementary Video 6), while a total of 1,400 RBCs are captured within 80 ms (refer to the rendered time-lapse video in Supplementary Video 7). Therefore, we have reached a throughput of approximately 20,940 cells/second for Jurkat T cells and a throughput of 17,500 cells/second for mouse RBCs. Note that our demonstrated cell measurement throughput is 100-1000 times faster than current 3D cell imaging methods.

By segmenting the cells from their 3D RI maps, we can extract multiple morphological and biophysical parameters, as well as the dry mass that reflects the total cell protein content. The distributions of these quantities in the entire cell population could be subsequently used for cell characterization and classification. As a proof-of-concept study, we extracted the mean RI, volume, surface area, and dry mass of the captured NIH/3T3 cells, Jurkat T cells, and mouse RBCs and explored their distributions for differentiating the cell populations. For each cell type, 500 cells are randomly chosen from the corresponding cell population as captured in the 3D time-lapse videos. From volume & surface area distribution (Fig. 3d), as expected the cell sizes from small to large are mouse RBCs, Jurkat T cells, and NIH/3T3 cells. We also noticed that mouse RBCs and Jurkat T cells are more concentrated in a narrow region than NIH/3T3 cells do. Such a difference is also expected as NIH/3T3 cells may come at different growth stages, while RBCs and Jurkat T cells are mature cells possessing more uniformly distributed cell sizes. In Fig. 3e, we plot dry mass & volume distribution, where the three cell types are well separated. The linear relationships of dry mass vs. volume indicate that NIH/3T3 cells and mouse RBCs have similar RI mean values, while Jurkat T cells' RI values are slightly lower. To further characterize the cells using the 3D shape information, the correlations between mean RI and volume-to-area ratio, as well as dry mass and mean RI, are explored as presented in Fig. 3f-g, where a clear separation of all the three cell types is observed. The details for computing mean RI, volume, surface area, and dry mass and their distributions are elaborated in *Supplementary Material*, Section S8.

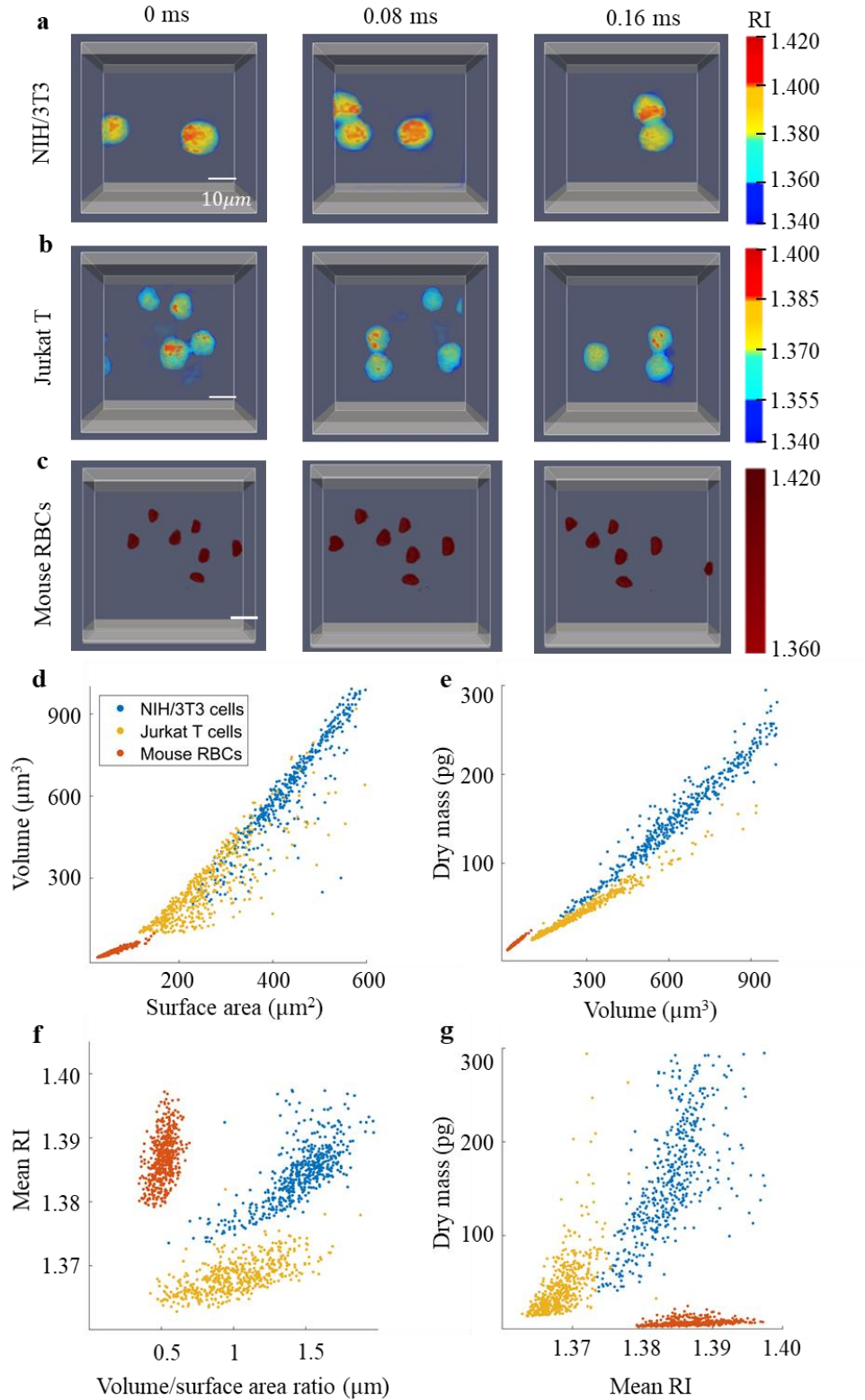


Figure 3. Demonstration of SILACT as a high-throughput and high-content 3D imaging flow cytometer. 3D rendering of the imaged (a) NIH/3T3 cells, (b) Jurkat T cells, and (c) mouse RBCs at different time points as they flow through the channels, respectively. The flow velocities of the NIH/3T3 cells, Jurkat T cells, and mouse RBCs are 0.46 m/sec, 0.31 m/sec, and 0.33 m/sec, respectively. The imaging speed is 12.5k vps. (d)-(g), the scatter plots of (d) surface area vs. volume, (e) volume vs. dry mass, (f) volume/surface area ratio vs. mean RI, and (g) mean RI vs. dry mass. The data from NIH/3T3 cells, Jurkat T cells, and mouse RBCs are shown with blue dots, orange dots, and red dots in (e)-(g).

2.5 Observing Red Blood Cell deformation

As illustrated in the scheme of shear force-induced RBC deformation in Fig S9f, the RBCs in the microfluidic channel (see *Supplementary Material*, Sections S10 and S11) can be deformed by increasing shear rates when they float from wider to narrower regions (a process similar to RBCs travelling in capillaries in human). In our RBC experiment, the flow velocity is 0.33 m/sec, and the 3D image acquisition speed is 10,000 vps. The entire process of RBC deformation is captured by SILACT for a total of 5 ms, and a time-lapse video is created for visualizing the whole process (see *Supplementary Video 8*). Volumetric renderings of selected frames are shown in Fig. 4a. The ML engine used for the results in this section was trained with a dataset of ~500 input-ground truth pairs of human RBCs with PCC approaching ~0.96 on test samples. We also trained the ML engine with NIH/3T3 cells and compared the RBC results with the current results (refer to the details in *Supplementary Material*, Section S9). The RBC results trained with NIH/3T3 are slightly worse with PCC drops to ~ 0.88, while the extracted morphological parameters remain similar, which further supports the generalization capability of SILACT.

Figure 4b quantifies the evolution of a selected RBC's eccentricity (formula in *Supplementary Material*, Section S8) as it drifts into the region of higher shear rate in the microfluidic channel. As expected, the RBC gets elongated as it flows through the transition region, and it stabilizes after completely entering the narrower section of the channel.

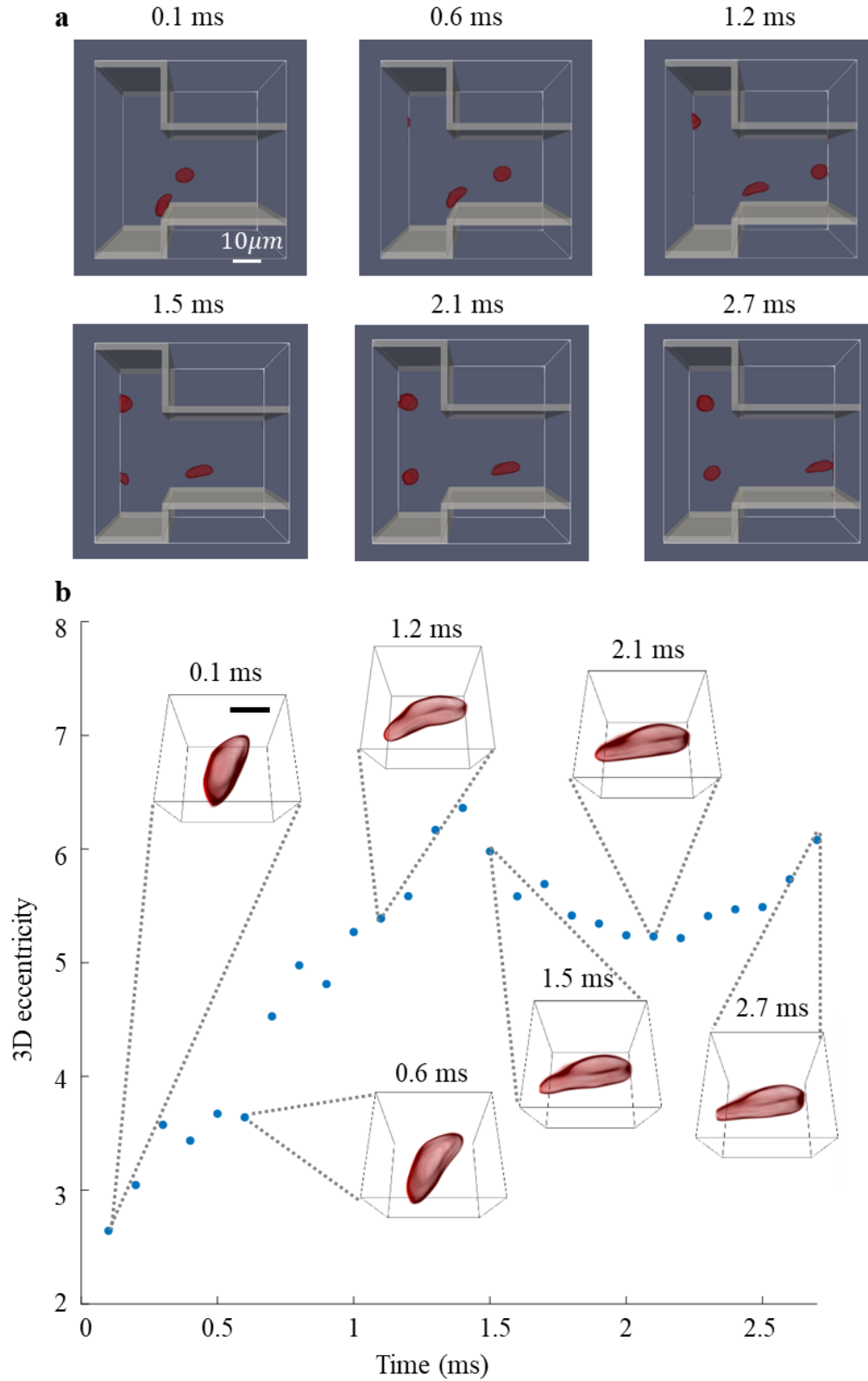


Figure 4. Demonstration of SILACT for 3D visualization of RBC deformation in a microfluidic channel. (a) 3D renderings of the RBCs flowing in the microfluidic channel at time points of 0.1, 0.6, 1.2, 1.5, 2.1 and 2.7 ms. (b) variation of the 3D eccentricity of a selected RBC over time (0-2.7 ms). 3D renderings of the selected RBC at time points 0.1, 0.6, 1.2, 1.5, 2.1, and 2.7 ms are embedded into this figure. The complete flow process for a total of 5 ms is provided in Supplementary Video 8.

3. Discussion

SILACT's performance is based on a careful system-level coordination of our two key design choices: multiplex illumination with four angles, a fairly small number, to obtain the raw images; and a physics-incorporating ML engine which converts the raw images to Phase Approximants and finally to 3D RI maps. The battery of tests described in the previous sections and in the *Supplementary Material* is meant to validate 3D RI map fidelity despite operating the instrument aggressively at tens of thousands of volumes per second. Concerns about ML, in particular, are often well-justified when the parameters of an algorithm are determined not from first principles directly but rather from numerical optimization—this is the infamous “black box” problem. Traditional compressed sensing algorithms (47–49) often come under similar criticism. In our case, by incorporating the Phase Approximant as a prior from instrument physics and the Learning-to-Synthesize scheme for spatial frequency rebalancing, we have mitigated the black box concern explicitly. Besides, ML also enhances the spatial resolution of our method for better resolving the intracellular structures and more accurately extracting the morphological parameters.

To facilitate more applications in biology laboratories and clinical practice, several straightforward modifications may be readily implemented into SILACT to significantly decrease system cost and footprint. For example, multiplex illumination using DMDs can be replaced with a fibre coupler with four output ends. System cost can be further cut by replacing the high-speed camera with a cost-effective Universal Serial Bus (USB) camera, while high-speed 3D imaging at >100 vps can still be realised to meet many biomedical imaging requirements, thanks to the single-frame 3D imaging capability of SILACT. The algorithm is also amenable to improvements, e.g., implementing transfer learning (50) to further broaden the diversity of cells we can reconstruct reliably. Furthermore, as the 3D RI maps reconstructed by SILACT contain rich information in both morphology and biochemical content of the cells, ML-based image classification could facilitate cell discrimination in blood testing (e.g., circulating tumour cell detection and leukocyte sub-type differential counting), drug screening, etc.

4. Methods

Here, we elaborate on the basic principles of the SILACT experimental platform and algorithmic pipeline introduced briefly in section 2.1. Section 4.1 describes the interferometric microscope apparatus that acquires multiplex interferograms with a high-speed camera. Section 4.2 discusses the estimation of Phase Approximants from the multiplex interferogram. The design of LS-DNN and training strategy for SILACT's ML engine are provided in Section 4.3. The technical descriptions of Sections 4.1-3 are also graphically summarized in Fig. 5. Brief technical introductions to alternative ODT methods *vis-à-vis* SILACT are in section 4.4. Cell preparation protocols are described in Section 4.5. Additional technical details and analysis of experimental results are in *Supplementary Material*.

4.1 High-speed angle-scanning and angle-multiplex interferometric microscope

The schematic of the interferometric microscope apparatus used in SILACT is shown in Fig. 5a. A 532 nm laser (CNI Lasers, MGL-III-532-300mW) is used as the illumination source. The laser beam is divided into two beams by a 1×2 Single-Mode Fibre Coupler (SMFC). One beam serves as the reference for interferometric detection, while the other is directed to the sample. The sample beam is collimated by a lens L1 ($f_1 = 200$ mm) before impinging onto DMD D1 (Texas Instruments Inc., DLP LightCrafter 9000), which is programmed for displaying Lee hologram patterns consisting of multiple diffracted plane waves. Lens L2 ($f_2 = 150$ mm) enables these reflected beams to form a series of diffraction spots at the Fourier plane, where the second DMD2 (Texas Instruments Inc., DLP LightCrafter 6500) is placed. The filter mask patterns shown in inset 1 of the figure are loaded onto DMD2 to block spurious diffraction orders and only allow downstream the desired 1st diffraction order. Next, the filtered beam is collimated by lens L3 ($f_3 = 200$ mm), followed by a $4f$ system composed of a tube lens L4 ($f_4 = 300$ mm) and an objective lens OL1 (Zeiss, 63X/1.3, water immersion). The $4f$ system magnifies the angular range of the sample beam. After incidence on the sample, the scattered light is collected by the objective lens OL2 (Zeiss, 63X/1.25, oil immersion), then reflected by mirror M1 and collimated by lens L5 ($f_5 = 150$ mm). A Beam Splitter (BS) behind lens L5 combines the sample and the reference beams into the multiplex interferogram, which is spatially magnified by the $4f$ system consisting of lens L6 ($f_6 = 60$ mm) and L7 ($f_7 = 400$ mm). The resulting raw image is captured by a high-speed camera (Photron, Fastcam SA-X2).

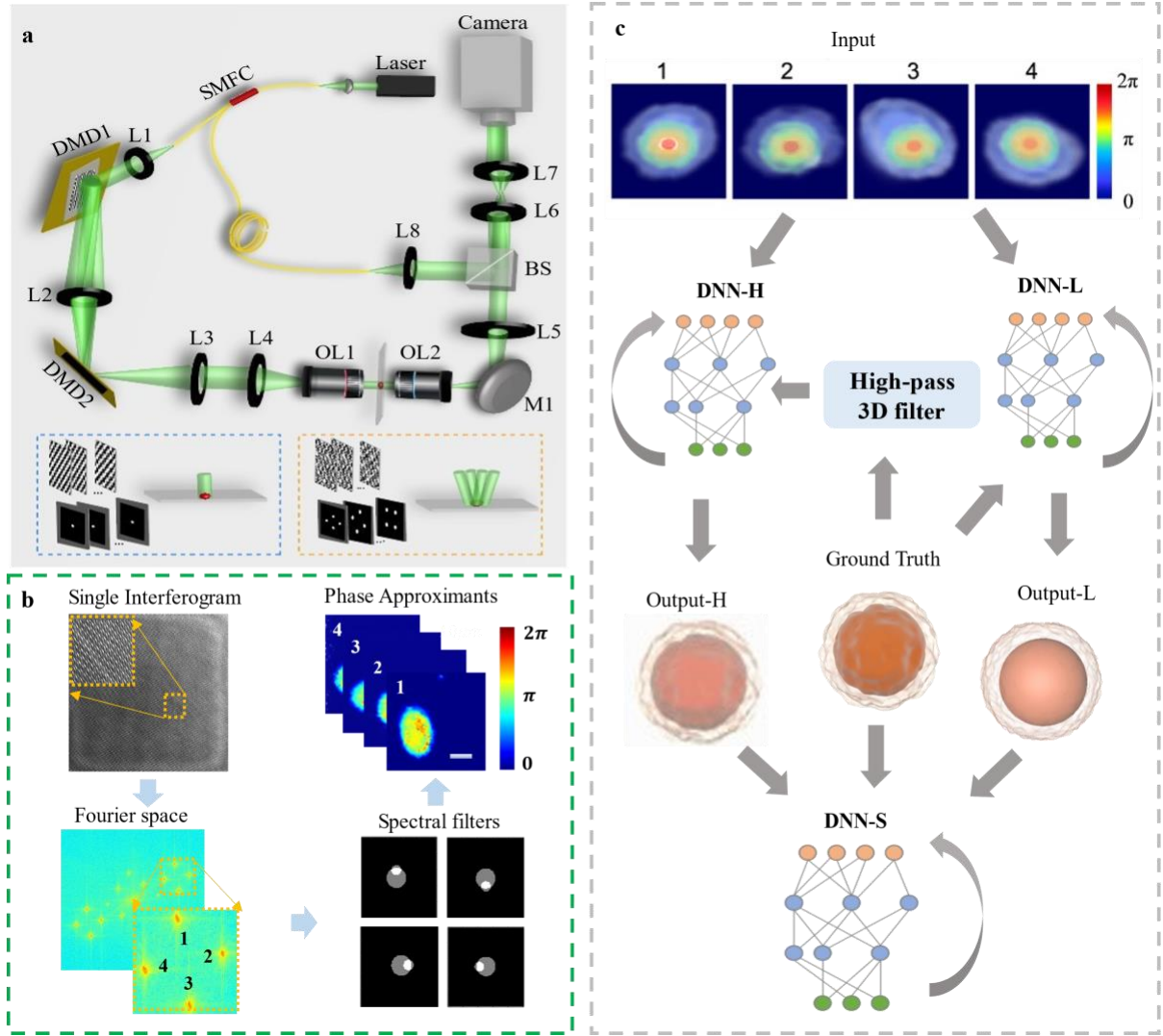


Figure 5. Detailed depiction of the operation of SILACT. (a) System design of SILACT and illustration of single illumination and multiplex illumination. (b) Pipeline of the spectral filtering method for acquiring the Phase Approximants. (c) Flow chart of the two-step training process for LS-DNN.

4.2 Phase Approximant retrieval

The multiplex interferogram is first spatially Fourier transformed as illustrated in Fig. 5b. Nine bright spots can be seen near the central region of the Fourier space. The central spot is the 0th diffraction order or Direct Current (DC) order, while the other eight spots are pairwise cross-correlations of the four scattered beams and the reference beam. The top right and bottom left regions are the +1st and -1st orders which correspond to interference between each one of the four scattered beams and the reference beam. To extract the phase maps of the four illumination angles individually, four specially designed spectral filters are digitally applied to the +1st order. The retrieved Phase Approximants are shown in Fig. 5b. The mathematical formulation of the interferogram and the retrieval of the Phase Approximants are in the *Supplementary Material*, Section S1.

4.3 Learning to Synthesize by DNN

Our motivation to develop this technique is based on earlier observations that 2D reconstructions by machine learning often exhibit deficiencies at the high end of the spatial frequency spectrum. This has been attributed to the relative sparsity of high frequencies in training databases (38). To compensate, the two-step LS-DNN algorithm splits the spectral information into two bands, high and low, processes them separately, and then recombines. This requires three DNNs, which are trained separately, as shown in Fig. 5c: one trained for the high-frequency bands, DNN-H; one trained for the low-frequency bands, DNN-L; and a final “synthesizer” DNN-S trained to output the compensated reconstruction exhibiting even fidelity at all frequency bands (45).

Here, we modified the previously 2D-oriented LS principle (45) to work for 3D RI reconstruction from Phase Approximants, as follows. Let $n(x, y, z)$ denote the RI map in the Cartesian coordinates (x, y, z) with $z = 0$ corresponding to the centre of the reconstructed 3D RI map. In SILACT, the ground truth 3D RI maps contain 100 layers along the z -direction, and the interval between adjacent layers is $0.21 \mu\text{m}$. As the cells that we use are mostly confined to a small axial dimension within $|z| \leq 8 \mu\text{m}$ (equivalently to 80 layers), and in the cell support most sub-cellular features are located within $|z| \leq 6 \mu\text{m}$ (i.e., the region where high frequencies are of the highest significance). In the region $6 \mu\text{m} < |z| \leq 8 \mu\text{m}$, relatively fewer fine details of the cells are present, whereas in the region $|z| > 8 \mu\text{m}$ is typically void. Accordingly, we define the spatial filter as:

$$M(k_x, k_y; z) = \begin{cases} 1, & |z| > 8\mu\text{m} \text{ (no filtering)} \\ (k_x^2 + k_y^2)^{0.8}, & 6\mu\text{m} < |z| \leq 8\mu\text{m} \text{ (moderate filtering)} \\ (k_x^2 + k_y^2)^{1.5}, & |z| \leq 6\mu\text{m} \text{ (strong filtering)} \end{cases} \quad (1)$$

Let $F(\cdot)$ denote the Fourier transform operator. We produce filtered RI functions $\tilde{n}(x, y, z) = F^{-1}(F(n(x, y, z))M(k_x, k_y; z))$ for use in the DNN-H pipeline, both training and in actual operation. For the DNN-L pipeline, we use the unfiltered $n(x, y, z)$. The DNNs are trained separately in the supervised mode, as in the previous work of 2D LS-DNN (45).

The aforementioned LS-DNN architecture works well for the training of NIH/3T3 cells as we discussed earlier in Section 2. Although the ML engine trained with only NIH/3T3 cells has satisfactory generalization ability, training on other species of cells is sometimes necessary to further improve the performance of SILACT. For example, we can fine tune the hyperparameters in the NIH/3T3 cell trained DNN model by training on a small number of other cell species (e.g., transfer learning). Since different types of cells have various cellular structures, our training strategies on different species of cells are distinct. For example, RBCs have simpler structures and smaller sizes than NIH/3T3 cells. Therefore, we could only use the input-ground truth pairs of RBCs to train DNN-L (Section S9, *Supplementary material*). Furthermore, the hyperparameters of the high-pass filters can be changed to accommodate the training of different species of cells.

To design SILACT's ML engine, we used a dataset consisting of 900 input ensembles obtained from NIH/3T3 cells. Each ensemble consists of four Phase Approximants estimated from the corresponding multiplex interferogram and the ground truth for the same scene, *i.e.*, the 3D RI map reconstructed from 49 true phase maps with LT-BPM (see *Supplementary Material*, Sections S2&S3). From the dataset, 5% of the ensembles are used for validation and a further 39 disjoint ensembles are reserved for testing. The remaining ensembles are used for training. For the results shown in Section 2.5, the same procedure is carried out but with RBCs instead of NIH/3T3 cells.

The training loss function is the Negative Pearson Correlation Coefficient (NPCC), defined as:

$$\text{NPCC}(n, \hat{n}) = - \frac{\sum_i (n_i - \bar{n})(\hat{n}_i - \bar{\hat{n}})}{\sqrt{\sum_i (n_i - \bar{n})^2 \sum_i (\hat{n}_i - \bar{\hat{n}})^2}} \quad (2)$$

where n and \hat{n} are the ground truth and the output of a neural network, respectively; \bar{n} and $\bar{\hat{n}}$ are their means; and i indexes the voxels. This choice has been previously proven capable of reconstructing fine features with good fidelity (38). NPCC is invariant under linear transformations, *i.e.*, $\text{NPCC}(n, \hat{n}) = \text{NPCC}(n, a\hat{n} + b)$ for all a and b values. Therefore, to obtain RI distributions at the correct scale, in the validation examples we linearly fit the training ground truth to the neural network output and estimate the coefficients α_1 and α_2 from the least squares (refer to *Supplementary Material*, Section S7). The estimated values of α_1 and α_2 are then fixed for the subsequent operation in SILACT, and the final quantitative 3D RI map is produced as $\hat{n}_{\text{final}}(x, y, z) = \alpha_1 \hat{n}(x, y, z) + \alpha_2$.

4.4. Cell preparation

COS-7, HeLa, NIH/3T3, HEK293T, and Jurkat T cell lines are obtained from American Type Culture Collection (ATCC) and tested free of mycoplasma contamination. COS-7, HeLa, NIH/3T3 and HEK293T cells are cultured in a 6-well plate (SPL) and immersed in high-glucose DMEM (Gibco), supplemented with 10% fetal bovine serum (Gibco) and 1% penicillin-streptomycin (Gibco). Jurkat T cells were cultured in RPMI 1640 medium (Gibco), supplemented with 10% fetal bovine serum (Gibco) and 1% penicillin-streptomycin (Gibco). Cells are passaged every 2–3 days and are incubated at 37°C in a humidified atmosphere containing 5% CO₂.

For live-cell imaging, cells are plated in 50 mm ibidi μ -dish with ibiTreat (Ibidi) at 2500 cells/cm² with a 24-hour long growth. Two hours before imaging, the debris and non-attached cells are removed and washed gently by 1x sterile phosphate buffer saline (PBS). Finally, complete cell growth medium is added for live-cell imaging.

Red blood cell collection: BALB/c mice are maintained by the Laboratory Animal Service Centre, The Chinese University of Hong Kong, Shatin, Hong Kong SAR. All animal procedures are conducted with the approval of the Animal Experimentation Ethics Committee (Ref. No.: 18/233/MIS) of The Chinese University of Hong Kong and the Department of Health, the Government of the HKSAR under the Animals (Control of Experiments) Ordinance, Chapter 340 (18–522 in DH/SHS/8/2/1 Pt.12 and 18–523 in DH/SHS/8/2/1 Pt.12). For the withdrawal of blood, the mouse is first restrained, and approximately 100 μ L blood is collected from the saphenous vein by puncturing with a 25 AWG needle (Becton Dickinson) to a heparinized capillary tube. The collected blood is then washed twice with PBS by centrifugation at $500 \times g$ for 5 min and pellets of RBCs are obtained. Finally, the supernatant is discarded, and RBCs are resuspended with PBS and ready for subsequent experiments.

Expired human RBCs (HA RE001F3) are aspirated from a 200 mL unit of packed RBCs using 23 AWG needle in a 1 mL syringe (Becton Dickinson) and washed twice with PBS by centrifugation $500 \times g$ for 5 min to obtain the pellet of human RBCs. The isolated RBCs are then resuspended in PBS for subsequent experiments.

All investigations are conducted with freshly isolated RBCs (within 4 hours from the collection either from mice or human blood unit). All centrifugations to isolate RBCs are conducted at 4 °C using a high-speed refrigerated centrifuge (Neo-fuge 13 R, Heal Force).

References

1. M. Boutros, F. Heigwer, C. Laufer, Microscopy-Based High-Content Screening. *Cell* **163**, 1314–1325 (2015). doi: 10.1016/j.cell.2015.11.007.
2. P. O. Krutzik, G. P. Nolan, Fluorescent cell barcoding in flow cytometry allows high-throughput drug screening and signaling profiling. *Nat. Methods* **3**, 361–368 (2006). doi: 10.1038/NMETH872.
3. P. O. Krutzik, J. M. Crane, M. R. Clutter, G. P. Nolan, High-content single-cell drug screening with phosphospecific flow cytometry. *Nat. Chem. Biol.* **4**, 132–142 (2008). doi: 10.1038/nchembio.2007.59.
4. A. M. Newman *et al.*, Determining cell type abundance and expression from bulk tissues with digital cytometry. *Nat. Biotechnol.* **37**, 773–782 (2019). doi: 10.1038/s41587-019-0114-2.
5. E. Porpiglia *et al.*, High-resolution myogenic lineage mapping by single-cell mass cytometry. *Nat. Cell Biol.* **19**, 558–567 (2017). doi: 10.1038/ncb3507.
6. N. Nitta *et al.*, Intelligent Image-Activated Cell Sorting. *Cell* **175**, 266–276 (2018). doi: 10.1016/j.cell.2018.08.028.
7. Y. K. Park *et al.*, Measurement of red blood cell mechanics during morphological

- changes. *Proc. Natl. Acad. Sci. U. S. A.* **107**, 6731–6736 (2010). doi: 10.1073/pnas.0909533107.
8. P. Hosseini *et al.*, Cellular normoxic biophysical markers of hydroxyurea treatment in sickle cell disease. *Proc. Natl. Acad. Sci. U. S. A.* **113**, 9527–9532 (2016). doi: 10.1073/pnas.1610435113.
 9. P. Rosendahl *et al.*, Real-time fluorescence and deformability cytometry. *Nat. Methods* **15**, 355–358 (2018). doi: 10.1038/nmeth.4639.
 10. J. Thachil, I. Bates, in *Dacie and Lewis Practical Haematology: 12th Edition*, Chapter 23 (2017).
 11. M. Urbanska, P. Rosendahl, M. Kräter, J. Guck, High-throughput single-cell mechanical phenotyping with real-time deformability cytometry. *Methods Cell Biol.* **147**, 175–198 (2018). doi: 10.1016/bs.mcb.2018.06.009.
 12. H. S. Park *et al.*, Quantitative phase imaging of erythrocytes under microfluidic constriction in a high refractive index medium reveals water content changes. *Microsystems Nanoeng.* **5**, 63 (2019). doi:10.1038/s41378-019-0113-y.
 13. H. S. Park, S. Ceballos, W. J. Eldridge, A. Wax, Invited Article: Digital refocusing in quantitative phase imaging for flowing red blood cells. *APL Photonics* **3**, 110802 (2018). doi:10.1063/1.5043536.
 14. Y. K. Park *et al.*, Refractive index maps and membrane dynamics of human red blood cells parasitized by *Plasmodium falciparum*. *Proc. Natl. Acad. Sci. U. S. A.* **105**, 13730–13735 (2008). doi: 10.1073/pnas.0806100105.
 15. D. L. Coutu, K. D. Kokkaliaris, L. Kunz, T. Schroeder, Multicolor quantitative confocal imaging cytometry. *Nat. Methods* **15**, 39–46 (2018). doi: 10.1038/nmeth.4503.
 16. H. Choi, D. N. Wadduwage, T. Y. Tu, P. Matsudaira, P. T. C. So, Three-dimensional image cytometer based on widefield structured light microscopy and high-speed remote depth scanning. *Cytom. Part A* **87**, 49–60 (2015). doi: 10.1002/cyto.a.22584.
 17. Y. Han, Y. Gu, A. C. Zhang, Y. H. Lo, Review: Imaging technologies for flow cytometry. *Lab Chip* **16**, 4639–4647 (2016). doi: 10.1039/C6LC01063F.
 18. K. C. M. Lee *et al.*, Quantitative Phase Imaging Flow Cytometry for Ultra-Large-Scale Single-Cell Biophysical Phenotyping. *Cytom. Part A* **95**, 510–520 (2019). doi: 10.1002/cyto.a.23765.
 19. S. H. Cho *et al.*, Review Article: Recent advancements in optofluidic flow cytometer. *Biomicrofluidics* **4**, 043001 (2010). doi: 10.1002/cyto.a.23765.
 20. E. J. Gualda, H. Pereira, G. G. Martins, R. Gardner, N. Moreno, Three-dimensional imaging flow cytometry through light-sheet fluorescence microscopy. *Cytom. Part A* **91**, 144–151 (2017). doi: 10.1002/cyto.a.23046.
 21. M. Muller, *Introduction to confocal fluorescence microscopy* (SPIE Press, 2006).
 22. R. M. Power, J. Huisken, A guide to light-sheet fluorescence microscopy for multiscale imaging. *Nat. Methods* **14**, 360–373 (2017). doi: 10.1038/nmeth.4224.

23. B. C. Chen *et al.*, Lattice light-sheet microscopy: Imaging molecules to embryos at high spatiotemporal resolution. *Science* **346**, 1257998 (2014), doi:10.1126/science.1257998.
24. L. Shao, P. Kner, E. H. Rego, M. G. L. Gustafsson, Super-resolution 3D microscopy of live whole cells using structured illumination. *Nat. Methods* **8**, 1044–1048 (2011). doi: 10.1038/nmeth.1734.
25. W. Choi *et al.*, Tomographic phase microscopy. *Nat. Methods* **4**, 717–719 (2007). doi: 10.1038/nmeth1078.
26. D. Jin, R. Zhou, Z. Yaqoob, P. T. C. So, Tomographic phase microscopy: principles and applications in bioimaging [Invited]. *J. Opt. Soc. Am. B.* **34**, B64-B77 (2017). doi: 10.1364/JOSAB.34.000B64.
27. Y. Han *et al.*, Cameraless high-throughput three-dimensional imaging flow cytometry. *Optica* **6**, 1297-1304 (2019). doi: 10.1364/OPTICA.6.001297.
28. C. Bai *et al.*, 3D Imaging Restoration of Spinning-Disk Confocal Microscopy Via Deep Learning. *IEEE Photonics Technol. Lett.* **32**, 1131–1134 (2020). doi: 10.1109/LPT.2020.3014317.
29. E. Auksoorius *et al.*, In vivo imaging of human cornea with high-speed and high-resolution Fourier-domain full-field optical coherence tomography. *Biomed. Opt. Express* **11**, 2849–2865 (2020). doi: 10.1364/BOE.393801.
30. K. Yanny *et al.*, Miniscope3D: optimized single-shot miniature 3D fluorescence microscopy. *Light Sci. Appl.* **9**, 171 (2020), doi:10.1038/s41377-020-00403-7.
31. J. K. Adams *et al.*, Single-frame 3D fluorescence microscopy with ultraminiature lensless FlatScope. *Sci. Adv.* **3**, e1701548 (2017). doi: 10.1126/sciadv.1701548.
32. Y. Sung *et al.*, Size homeostasis in adherent cells studied by synthetic phase microscopy. *Proc. Natl. Acad. Sci. U. S. A.* **110**, 16687–16692 (2013). doi: 10.1073/pnas.1315290110.
33. S. E. Boddington *et al.*, Labeling Human Mesenchymal Stem Cells with Fluorescent Contrast Agents: the Biological Impact. *Mol. Imaging Biol.* **13**, 3–9 (2010). doi: 10.1007/s11307-010-0322-0.
34. D. Ganini *et al.*, Fluorescent proteins such as eGFP lead to catalytic oxidative stress in cells. *Redox Biol.* **12**, 462–468 (2017). doi: 10.1016/j.redox.2017.03.002.
35. T. Kim *et al.*, White-light diffraction tomography of unlabelled live cells. *Nat. Photonics* **8**, 256–263 (2014). doi: 10.1038/nphoton.2013.350.
36. D. Jin, R. Zhou, Z. Yaqoob, P. T. C. So, Dynamic spatial filtering using a digital micromirror device for high-speed optical diffraction tomography. *Opt. Express* **26**, 428-437 (2018). doi: 10.1364/OE.26.000428.
37. H. Wang *et al.*, Deep learning enables cross-modality super-resolution in fluorescence microscopy. *Nat. Methods* **16**, 103–110 (2019). doi: 10.1038/s41592-018-0239-0.
38. S. Li, G. Barbastathis, Spectral pre-modulation of training examples enhances the spatial resolution of the phase extraction neural network (PhENN). *Opt. Express* **26**, 29340-

- 29352 (2018). doi: 10.1364/OE.26.029340.
39. A. Goy, K. Arthur, S. Li, G. Barbastathis, Low Photon Count Phase Retrieval Using Deep Learning. *Phys. Rev. Lett.* **121**, 243902 (2018). doi: 10.1103/PhysRevLett.121.243902.
 40. C. Ounkomol, S. Seshamani, M. M. Maleckar, F. Collman, G. R. Johnson, Label-free prediction of three-dimensional fluorescence images from transmitted-light microscopy. *Nat. Methods* **15**, 917–920 (2018). doi: 10.1038/s41592-018-0111-2.
 41. K. Kim *et al.*, High-resolution three-dimensional imaging of red blood cells parasitized by Plasmodium falciparum and in situ hemozoin crystals using optical diffraction tomography. *J. Biomed. Opt.* **19**, 011005 (2013). doi: 10.1117/1.JBO.19.1.011005.
 42. Y. He, Y. Wang, R. Zhou, Digital micromirror device based angle-multiplexed optical diffraction tomography for high throughput 3D imaging of cells. In *Emerging Digital Micromirror Device Based Systems and Applications XII* **11294**, 1129402 (2020). doi: 10.1117/12.2547017.
 43. U. S. Kamilov *et al.*, Optical Tomographic Image Reconstruction Based on Beam Propagation and Sparse Regularization. *IEEE Trans. Comput. Imaging* **2**, 59–70 (2016). doi: 10.1109/TCI.2016.2519261.
 44. U. S. Kamilov *et al.*, Learning approach to optical tomography. *Optica* **2**, 517-522 (2015). doi: 10.1364/OPTICA.2.000517
 45. M. Deng, S. Li, A. Goy, I. Kang, G. Barbastathis, Learning to synthesize: robust phase retrieval at low photon counts. *Light Sci. Appl.* **9**, 36 (2020), doi:10.1038/s41377-020-0267-2.
 46. S. Li, M. O. Deng, J. Lee, A. Sinha, G. Barbastathis, Imaging through glass diffusers using densely connected convolutional networks. *Optica* **5**, 803-813 (2018), doi:10.1364/OPTICA.5.000803.
 47. E. J. Candès, J. K. Romberg, T. Tao, Stable signal recovery from incomplete and inaccurate measurements. *Commun. Pure Appl. Math.* **59**, 1207–1223 (2006). doi: 10.1002/cpa.20124.
 48. D. L. Donoho, Compressed sensing. *IEEE Trans. Inf. Theory* **52**, 1289–1306 (2006). doi: 10.1109/TIT.2006.871582.
 49. D. J. Brady, *Optical Imaging and Spectroscopy* (John Wiley & Sons, 2008).
 50. S. J. Pan, Q. Yang, A survey on transfer learning. *IEEE Trans. Knowl. Data Eng.* **22**, 1345–1359 (2010). doi: 10.1109/TKDE.2009.191.

Acknowledgments

The authors gratefully acknowledge Mr. Subeen Pang (Mechanical Engineering Department, MIT) for useful discussions on the realisation of LT-BPM; Dr. Marianne M. Lee (School of Life Sciences, The Chinese University of Hong Kong) for assistance with the mouse studies; Dr. Nelson Tang (Department of Chemical Pathology, Faculty of Medicine, The Chinese University of Hong Kong) for providing the human RBCs; Mr. Michał Ziemczonok (Institute

of Micromechanics and Photonics, Warsaw University of Technology) for providing the 3D printed cell phantom samples; and Dr. Ulugbek Kamilov (Department of Computer Science and Engineering and Department of Electrical and Systems Engineering, Washington University in St. Louis) for providing the LT-BPM code.

Funding:

Croucher Innovation Awards 2019 grant CM/CT/CF/CIA/0688/19ay (R.Z., Y.H.)

Hong Kong Innovation and Technology Fund grant ITS/098/18FP, ITS/178/20FP, and ITS/148/20 (R.Z., Y.H.)

The Chinese University of Hong Kong Research Sustainability of Major RGC Funding Schemes – Strategic Areas (R.Z., Y.H.)

National Institutes of Health (NIH) grant 5-P41-EB015871-27, 5R21NS091982-02, and the Hamamatsu Corporation (B.G., Z.Y., P.T.C.S.)

Singapore–MIT Alliance for Research and Technology (SMART) Center, Critical Analytics for Manufacturing Personalized-Medicine (CAMP) Interdisciplinary Research Group (B.G., P.T.C.S., G.B.)

MathWorks Fellowship (B.G.)

NIH grant R01DA045549 and R21GM140613-02 (Z.Y., P.T.C.S.)

Research Grants Council of the Hong Kong Special Administrative Region, China project CUHK 14203919 and C5011-19GF (Y. P. H., H. R.)

VC Discretionary Fund, the Chinese University of Hong Kong project 8601014 (Y. P. H., H. R.)

Hong Kong Innovation and Technology Fund grant ITS/133/20 (M. K. C., Y. P. H., H. R.)

Intelligence Advanced Research Projects Activity (IARPA) grant FA8650-17-C-9113 (M.D., Z.W., G.B.)

Singapore–MIT Alliance for Research and Technology (SMART) Center, Retinal Analytics via Machine learning aiding Physics (RAMP) Intra-Create Thematic Grant (G.B.)

Author contributions:

R.Z., G.B., P.T.C.S., and B.G. conceived the idea of SILACT. Y.H. built the optical system, performed the experiments, and collected the data. B.G. implemented the algorithm for reconstructing the ground truth of 3D refractive index maps. M.D. and B.G. designed and trained the machine learning engine for SILACT. B.G. and Y.H. implemented the algorithms for retrieving the biophysical parameters and analysed the data. H.R. designed the microfluidic channel and supported the microfluidic-related experiments. Y.W. and Y.H. cultured the cells required for the experiments. Y.H. created the 3D renderings of the cell images and the videos.

B.G., Y.H., M.D., and R.Z. wrote the first draft of the manuscript. R.Z., G.B., and P.T.C.S. supervised the research. All authors contributed to commenting, reviewing, and revising the manuscript.

Conflict of Interest: A US provisional patent has been filed based on this work.

Data and materials availability: All data are available in the manuscript and the supplementary materials.